Ratiometric Luminescent Thermometry with Excellent Sensitivity over a Broad Temperature Range Utilizing Thermally-Assisted and Multiphoton Upconversion in Triply-Doped $La_2O_3:Yb^{3+}/Er^{3+}/Nd^{3+}$

Guojun Gao, Dmitry Busko, Ngei Katumo, Reetu Joseph, Eduard Madirov, Andrey Turshatov, Ian A. Howard,* and Bryce S. Richards*

A ratiometric optical thermometer based on triply-doped $La_2O_3:Yb^{3+}/Er^{3+}/Nd^{3+}$ microcrystals is reported with a relative sensitivity above 1% K^{-1} in the entire range from 300–700 K, and is between 1.8–0.7% K^{-1} over the range 290–833 K. The 825 nm upconversion (UC) emission from the Nd^{3+} $^4F_{5/2}$ level relies on thermally-assisted energy transfer from Yb^{3+}; thus, unusually, the near-infrared emission increases with increasing temperature in the relevant range. More typically, the two-photon 660 nm UC from Er^{3+} $^4F_{9/2}$ level decreases in intensity with increasing temperature due to increasing non-radiative rates. The variation of fluorescent intensity ratio between these emissions is amplified by their opposite responses to temperature change leading to excellent sensitivity. Concurrently, the different pathways for the temperature response in the two emitting ions enable the high sensitivity to be maintained over an atypically broad temperature range. The wide separation in wavelength means that a standard silicon-based monochrome camera with broad (inexpensive) band pass filters is sufficient to use this phosphor for thermography. The concept of combining thermally-activated UC with classical Stokes-shifted emission is demonstrated to provide combined features of excellent and broad-range sensitivity plus excellent repeatability. Materials based on this concept are very promising for optical thermometry.

1. Introduction

Non-contact optical thermometry, based for example on fluorescence intensity ratio (FIR) determination of thermally-coupled peaks in lanthanide ions,[1] has attracted significant attention. Optical thermometry is preferable to traditional contact thermometry for certain applications because no direct contact is required, it can be self-referencing, it can provide high spatial resolution (when combined with an imaging optical system), it can have a rapid response, and is in general non-invasive in operation.[1e,2]

FIR optical thermometry typically relies on a pair of thermally-coupled levels (TCLs) in a lanthanide ion. The intensity ratio of the emission from higher TCL to the lower one varies with temperature due to the Boltzmann distribution of excited-states between the two levels: $\mathrm{FIR} = \frac{I_2}{I_1} = B\exp\left(-\frac{\Delta E_{21}}{k_B T}\right)$, where the B is a fitting parameter and ΔE_{21} is the separation between the pair of energy levels.[3] The sensitivity of the thermometer, defined as $S_a = \left|\frac{\partial \mathrm{FIR}}{\partial T}\right|$, and the relative sensitivity, $S_r = \left|\frac{1}{\mathrm{FIR}} \times \frac{\partial \mathrm{FIR}}{\partial T}\right|$, can easily be derived for TCLs as $S_a = \mathrm{FIR}\,\frac{\Delta E_{21}}{k_B T^2}$ and $S_r = \frac{\Delta E_{21}}{k_B T^2}$. Given that the energy levels of lanthanide ions are hardly affected by the host material, neither the energy gap nor the S_r based on emission from given pair of TCLs are affected much by the choice of host. In order to achieve a TCL-based ratiometric thermometer working at above room-temperature with a high S_r, energy gaps around 2000 cm^{-1} are optimal (too large $\Delta E > 2000$ cm^{-1} leads to very weak coupling of TCLs).[4] For example the ΔE of 1750 cm^{-1} between the $^5D_1$ and $^5D_0$ levels of Eu^{3+} would lead theoretically to a S_r around 2.8% at 300 K,[5] similar to the 2.5% experimentally realized.[6] However, by 700 K the S_r drops to less than 0.5%.[5,6] Other lanthanide ions with appropriately spaced

Dr. G. Gao, Dr. D. Busko, N. Katumo, R. Joseph, E. Madirov, Dr. A. Turshatov, Dr. I. A. Howard, Prof. B. S. Richards
Institute of Microstructure Technology
Karlsruhe Institute of Technology
76344 Eggenstein-Leopoldshafen, Germany
E-mail: guojun.gao@polysecure.de; ian.howard@kit.edu

E. Madirov
Institute of Physics
Kazan Federal University
Kremlevskaja str. 18, Kazan 420008, Russia

Dr. I. A. Howard, Prof. B. S. Richards
Light Technology Institute
Karlsruhe Institute of Technology
Engesserstrasse 13, 76131 Karlsruhe, Germany

The ORCID identification number(s) for the author(s) of this article can be found under https://doi.org/10.1002/adom.202001901.

DOI: 10.1002/adom.202001901

TCLs for high S_r are Tm^{3+} with a ΔE of ≈1750 cm^{-1} between the 660 nm and near-infrared (NIR) emissions of the $^3F_{2,3}$ and $^3H_4$ levels,[5] and Nd^{3+} with a ΔE ≈1895 cm^{-1} between the $^4F_{7/2}$ and $^4F_{3/2}$ levels.[7] Indeed, for Tm^{3+} an oxyfluoride glass ceramic experimental work has achieved a S_r of 3.0% at 300 K, again dropping to 0.5% by 700 K,[8] and similarly for Nd^{3+} in $NaYF_4$ the S_r decreases from ≈3% to ≈0.5% by 700 K.[9] Beyond the disadvantage of the decrease in S_r with the inverse of temperature squared for optical thermometers based solely on the TCLs of lanthanide ions, often the two emissions from the TCLs are not widely separated enough in wavelength to enable facile separation in low-cost technical implementations operating under real-world conditions.[4a]

To avoid such limitations, a recent strategy of using different thermal quenching behaviors of separate luminescent centers has been investigated.[4a,10] Via this strategy, not only can the spectral overlap be avoided, but also higher S_r over a broader range can be obtained. For example, Wang and coworkers reported an optical thermometer based on Tb^{3+}/Pr^{3+} co-doped $NaGd(MoO_4)_2$ micro-crystals by using different thermal quenching behaviors of Pr^{3+}:$^1D_2 \rightarrow ^3H_4$ and Tb^{3+}:$^5D_4 \rightarrow ^7F_5$ emissions.[4a] High S_r values between 1–2% K^{-1} over the temperature range from 350–475 K were obtained. Huang and coworkers reported on a high performance optical thermometer based on Eu^{2+}/Eu^{3+} co-doped Sc_2O_3 nanoparticles by using different thermal quenching behaviors of Eu^{2+}:5d→4f and Eu^{3+}:$^5D_0 \rightarrow ^7F_2$ emissions.[11] A maximum S_r value of 3.1% K^{-1} at 267 K was reported, based on the emission of Eu^{3+} (almost constant with temperature), versus Eu^{2+} (decreasing with temperature), but performance above room temperature was not investigated. Carlos and co-workers reported on Pr^{3+}-doped Sr_2GeO_4 microcrystals by capitalizing on different thermal quenching behaviors of Pr^{3+}:5d→4f and Pr^{3+}:$^3P_0 \rightarrow ^3H_4$ emissions.[12] This allowed them to develop a material with good performance over the impressive temperature range of 17–600 K. The maximum S_r value was an excellent 9.0% K^{-1} at 22 K, however from 300–600 K the S_r value remained below 1% K^{-1}.[12] Approaches have also been taken to isolate the different emission centers in different materials phases. For example, Dramićanin and coworkers recently presented results based on the ratio of emission between Mn^{4+} and Ho^{3+} in separate microcrystalline hosts (Mg_2TiO_4 and Y_2O_3, respectively) to yield a constant S_r of 4.6% K^{-1} between 300 and 370 K.[13] Recent work using emissions from the different activators in a mixture of nanoparticles singly-doped with Nd^{3+} or Eu^{3+} also allowed a constant S_r between 300 and 480 K, but at a value of less than 1.0% K^{-1}.[14] Expanding the possibilities beyond simple mixtures, dual-phase glass ceramics have been developed that exploit the different thermal quenching of Eu^{2+} and Cr^{3+}; this approach led to S_r decreasing only as $1/T$, but S_r in the measured range of in the range of 300–550 K was under 1% (calculated from the FIR fits presented in the paper).[10] Also, dual layer-thin films deposited by atomic layer deposition were very recently reported.[15] This approach again yielded S_r that did not exhibit the standard $1/T^2$ dependence, and a S_r of 3.6% K^{-1} at 640 K was achieved for the dual layer of YVO_4: Eu^{3+}, YVO_4: Dy^{3+}.[15]

Recently, we reported an optical thermometer based on TCLs of Nd^{3+}:$^4F_{7/2}/^4F_{5/2}$ in La_2O_3:Yb^{3+}/Nd^{3+} microcrystals over a very wide temperature range of 290–1200 K.[16] Therein, we studied the thermally-coupled levels Nd^{3+}:$^4F_{7/2}/^4F_{5/2}$, which displayed a S_r from 1.4% K^{-1} at 290 K decreasing to around 0.2% K^{-1} by 700 K. Interestingly though, the absolute emission from the Nd^{3+} was observed to increase due to the temperature-assisted nature of the energy transfer to the Nd^{3+} emitter from the Yb^{3+} sensitizer. The increase in intensity of this phonon-assisted upconversion (UC) process has also recently been observed and well characterized in Yb^{3+}/Nd^{3+} co-doped nanoparticles.[17] We have also reported that La_2O_3:Yb^{3+}/Er^{3+} microcrystals yield highly efficient UC emission in the 660 nm (Er^{3+}:$^4F_{9/2} \rightarrow ^4I_{15/2}$).[18] The La_2O_3:Yb^{3+}/Er^{3+} microcrystals demonstrated a high UC quantum yield of 3.8% when illuminated with a 980 nm laser with a low power density of 6.7 W/cm^2. At the same time, our related work on a laser-induced heating revealed strong thermal quenching of the 660 nm UC.[16,19] Inspired by the dual activator approaches reviewed in the literature above, we recognized that the intensity of the bright and easily-separable UC from Nd^{3+}:$^4F_{5/2} \rightarrow ^4I_{9/2}$ (≈840 nm) and Er^{3+}:$^4F_{9/2} \rightarrow ^4I_{15/2}$ (≈660 nm) depend oppositely on temperature variation, and hypothesized that combining these emission lines in a triply-doped material should lead to a unique UC ratiometric thermometer with high S_r over a broad range when excited with 980 nm NIR radiation.

2. Material Characterization

X-ray diffraction (XRD) analysis of the synthesized La_2O_3:$Yb^{3+}/Er^{3+}/Nd^{3+}$ (LYEN) materials shows that they conform to the trigonal A-type structure of Ln_2O_3 (lanthanides, space group: $P\bar{3}m1$ (164); ICSD No.: 100204) as shown in Figure S1, Supporting Information.[20] Fully consistent with our former publication, doping of smaller Yb^{3+} (92.5 pm, in sevenfold coordination) on La^{3+} sites (110 pm, in sevenfold coordination) in La_2O_3 lattice leads to two noticeable changes compared to undoped samples.[16,18] First, all diffraction peaks of La_2O_3 shift to higher angles that indicate the incorporation of Yb^{3+} in La_2O_3 lattice. Second, mild phase separation and a small amount of minor crystal phase of $LaYbO_3$ (space group: Pna21 (33); ICSD No.: 15093) can also be observed. The scanning electron microscope (SEM) image illustrates the irregular morphology of LYEN with particle size of 1–5 µm (see Figure S2, Supporting Information). The strong agglomeration of LYEN particles leads to the bigger clusters having size of 10–30 µm.

Typical absorption bands of Yb^{3+}, Er^{3+}, and Nd^{3+} can be observed in the diffuse reflectance spectrum of LYEN (see Figure S3, Supporting Information). The broad absorption band from 900 to 1050 nm, with a sharp peak at ≈980 nm and a shoulder at ≈934 nm, is ascribed to the transition of Yb^{3+}: $^2F_{7/2} \rightarrow ^2F_{5/2}$. The absorption bands with maxima at ≈438, 486, 536, 600, 638, 692, 750, 762, 822, and 902 nm are assigned to the electronic transitions of Nd^{3+} from the ground state of $^4I_{9/2}$ to the excited states of $^2P_{1/2}$, $^2G_{9/2}$, $^4G_{9/2} + ^4G_{7/2}$, $^4G_{5/2} + ^2G_{7/2}$, $^2H_{11/2}$, $^4F_{9/2}$, $^4S_{3/2}$, $^4F_{7/2}$, $^4F_{5/2}$, and $^4F_{3/2}$, respectively. The absorption bands with maxima at 522, 680, 798, and 980 nm are attributed to the electronic transitions of Er^{3+} from the ground state of $^4I_{15/2}$ to the excited states of $^4S_{3/2}$, $^4F_{9/2}$, $^4I_{9/2}$, and $^4I_{11/2}$, respectively.

3. Results and Discussion

Figure 1 illustrates the operational mechanisms that underpin this ratiometric thermometer. Bands around the 825 nm emission of the Nd^{3+}:$^4F_{5/2}$ level and the 660 nm emission of the Er^{3+}:$^4F_{9/2}$ level will be used to define the FIR. The Er^{3+}:$^4F_{9/2}$ level is populated by a two photon UC process.[18,21] The Yb^{3+}:$^2F_{5/2}$ and the Er^{3+}:$^4I_{11/2}$ are the intermediate states in this UC process, and in a simplified rate equation model can be considered as one communal population.[21] We note that the energy transfer from the Er^{3+}:$^4F_{9/2}$ level to Nd^{3+}:$^4F_{9/2}$ is theoretically possible but does not occur with the 2% doping of the activators present in our samples. As demonstrated below, the increase in the Nd^{3+}:$^4F_{5/2}$ emission with temperature shows that the thermally-assisted transfer from Yb^{3+}:$^2F_{5/2}$ is the dominant pathway populating this level.

The UC emission from Nd^{3+}:$^4F_{5/2}$ becomes brighter with temperature, given thermal energy is needed to bridge the energy gap between Nd^{3+}:$^4F_{5/2}$ and the Nd^{3+}:$^4F_{3/2}$ or Yb^{3+}:$^2F_{5/2}$ levels (these gaps are 1000 and 2300 cm^{-1} respectively). On the other hand, the Er^{3+}:$^4F_{9/2}$ is populated by two photon mechanisms that do not require thermal activation.[21] However, the non-radiative rate increases with temperature thus decreasing the 660 nm band emission. In Figure 1, we schematically show this as non-radiative transfer between Er^{3+}:$^4F_{9/2}$ and Er^{3+}:$^4I_{9/2}$ for simplicity, but this reduction can be thought to encompass all additional non-radiative losses from precursor levels.

The emission spectra of the UC emission of LYEN as a function of temperature (293–833 K) are plotted in **Figure 2**a. Upon excitation with a 980 nm laser, the UC emission profile of LYEN is composed of two distinct parts: i) red and ii) NIR. The UC emission in the range from 640 to 700 nm is assigned to the transition Er^{3+}:$^4F_{9/2}$ → $^4I_{15/2}$ (defined as "red"). Stark splitting causes the separation of the red UC emission of Er^{3+} into two bands with maxima at 663 and 672 nm. Both of these levels undergo thermal quenching behavior and their intensities gradually decrease with increasing temperature from 293 to 833 K. The total intensity of red UC at 833 K decreases by a factor of 12 compared to that at 293 K.

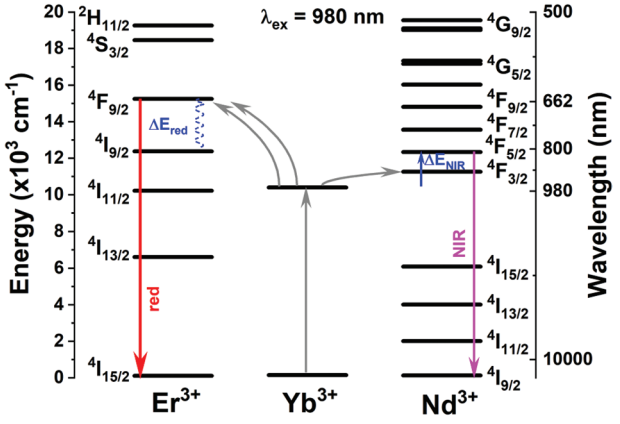

Figure 1. Energy level diagram schematically illustrating the opposite effect of temperature on the 660 nm Er^{3+} and 825 nm Nd^{3+} emission under 980 nm laser excitation of Yb^{3+}. The 660 nm Er^{3+}emission is thermally quenched due to increased non-radiative rates at higher temperatures. The NIR Nd^{3+} emission increases with temperature as thermal activation is required in order to allow energy transfer into these levels.

The broad emission in the range 740 to 860 nm (defined as "NIR"—see Figure 2a) is the result of UC of the Yb^{3+}/Nd^{3+} pair. There are two broad peaks having maxima at 762 and 825 nm, which are attributed to Nd^{3+}:$^4F_{7/2}$ → $^4I_{9/2}$ and Nd^{3+}:$^4F_{5/2}$ → $^4I_{9/2}$ transitions, respectively. The NIR UC intensity of Nd^{3+} increases with temperatures due to its single-photon, phonon-assisted UC nature. This is fully consistent with our recent publication.[16] Promisingly, at 833 K, a 65-fold enhancement of UC emission intensity for Nd^{3+} NIR band can be observed with respect to the initial intensity at 293 K.

The excellent separation between the UC emission of Er^{3+} and Nd^{3+} observable in Figure 2a is particularly noteworthy, as it makes the determination of the ratio with inexpensive optical filters easy and reliable. There is no spectral overlap between these two emissions, overcoming a problem commonly encountered in thermally-coupled levels. This wide separation between wavelengths is clearly advantageous when the phosphor is applied as a surface-coating (as demonstrated below). However, we do note that if the emitted light must travel through material (such as biological tissue) with difficult to determine and wavelength-dependent scattering properties such wide separation in wavelength becomes disadvantageous as the true FIR becomes corrupted by the different transmissions of the different emission wavelengths (which are difficult to accurately determine).[22]

The integrated intensity (over the areas shown in Figure 2a) of the red and NIR emissions are shown in Figure 2b, wherein the repeatability over two heating and cooling cycles is also illustrated by the 4 separate data points for each temperature in the range of 293–833 K. The overlay of experimental data points indicates the excellent repeatability during a thermal cycling over the whole temperature range.

In order to gain slightly more physical insight into the cause of the temperature dependency of the 660 nm and NIR emissions we also, for illustrative purposes, fit them to highly-simplified physical models. First, we consider the decrease in the 660 nm emission from the Er^{3+}:$^4F_{9/2}$ level. In the first order approximation, the increased rate of non-radiative decay from this level will decrease its emission. Expressing the total decay rate as the sum of a temperature independent radiative rate and a basic temperature dependent non-radiative rate,

$$k_{tot} = k_{rad} + k_{nr} \exp\left(-\frac{\Delta_{E_1}}{k_B T}\right) \quad (1)$$

(where k_{rad} is the radiative rate, k_{nr} is the exponential prefactor for the non-radiative rate, and Δ_{E_1} is the activation energy for the non-radiative rate), the quantum yield as a function of temperature is proportional to:

$$\frac{k_{rad}}{k_{rad} + k_{nr} \exp\left(-\frac{\Delta_{E_1}}{k_B T}\right)} = \frac{1}{1 + k_{nr}/k_{rad} \exp\left(-\frac{\Delta_{E_1}}{k_B T}\right)} \quad (2)$$

The collected emission intensity is proportional to the quantum yield (with the proportionality factor taking into account the excitation intensity and the fraction of the emitted

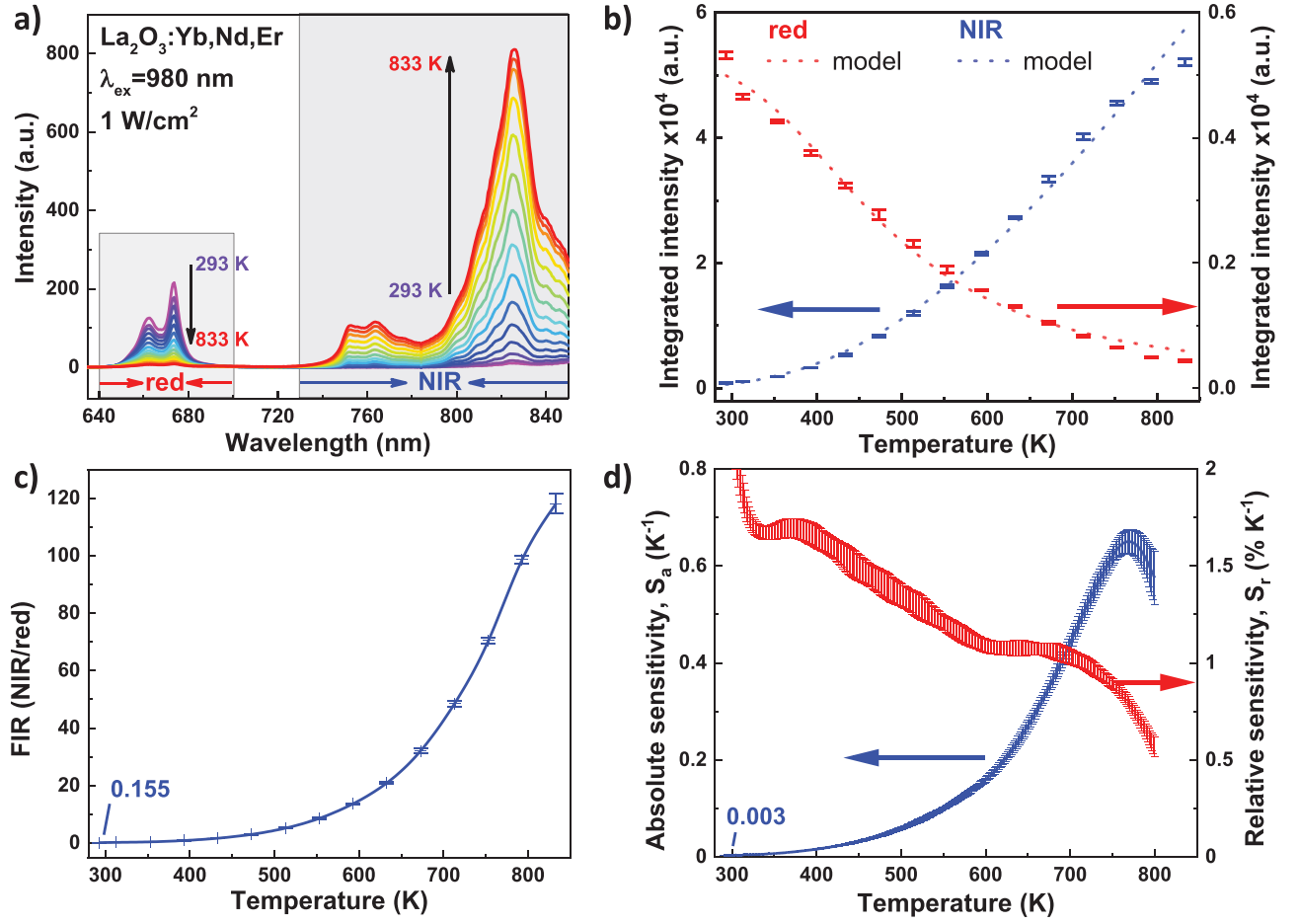

Figure 2. a) UC emission spectra of La_2O_3:6Yb^{3+},1Er^{3+},1Nd^{3+} as a function of temperature; b) integrated emission as function of temperature for red and NIR bands (2 heating–cooling cycles shown). Fits as discussed in text. c) FIR (I_{NIR}/I_{red}) based on the average red and NIR intensity over four measurements (2 heating–cooling cycles), line is spline guide to the eye. d) absolute (Sa) and relative (S_r) sensitivities interpolated through spline fit, uncertainties derived as discussed in supporting information. For all measurements the excitation power density was 1 W·cm^{-2} at 980 nm.

photons collected). Therefore the emitted intensity as a function of temperature can be expressed by Equation (3).[11]

$$I(T) = \frac{I_0}{1 + C\exp\left(-\frac{\Delta_{E_1}}{k_B T}\right)} \tag{3}$$

where I_0 is a fitting parameter that represents the emission intensity that would be collected at 0 K, C is a fitting parameter that corresponds to k_{nr}/k_{rad}, and Δ_{E_1} still represents the activation energy for the nonradiative rate. As shown in Figure 2b, the 660 nm emission intensity fits reasonably to such an expression (with a Δ_{E_1} of 1610 cm^{-1}).

In order to further check this hypothesis, in Figure S4, Supporting Information we show the Er^{3+}:$^4F_{9/2}$ lifetime as a function of temperature after direct excitation. Considering the above, an expression for the state lifetime can be derived that is simply a scaled form of the expression for the integrated emission:

$$\tau(T) = \frac{1}{k_{rad} + k_{nr}\exp\left(-\frac{\Delta_{E_1}}{k_B T}\right)} = \frac{1/k_{rad}}{1 + C\exp\left(-\frac{\Delta_{E_1}}{k_B T}\right)} \tag{4}$$

As shown in Figure S4, Supporting Information, the reduction in the lifetime of the Er^{3+}:$^4F_{9/2}$ state follows the same functional form as the decrease in the 660 nm emission in the thermometer, strongly supporting our hypothesis on the mechanistic understanding that the decrease in the 660 nm emission is mainly attributable to an increase in the non-radiative deactivation of the Er^{3+}:$^4F_{9/2}$ with increased temperature.

The lifetime of the Yb^{3+}:$^2F_{5/2}$ is also decreased as temperature increases. This lifetime as a function of temperature is displayed in Figure S5, Supporting Information. Whereas the lifetime of the Er^{3+}:$^4F_{9/2}$ level decreases by an order of magnitude from 300 to 800 K, the decrease of the Yb^{3+}:$^2F_{5/2}$ lifetime over the same temperature range is much less. At 800 K, the emission from Yb^{3+}:$^2F_{5/2}$ remains above 66% of its intensity at 300 K. The much smaller change in non-radiative rate compared to that of the Er^{3+}:$^4I_{9/2}$ is consistent with the much larger energy gap between Yb^{3+}:$^2F_{5/2}$ and Yb^{3+}:$^2F_{15/2}$ than the Er^{3+}:$^4F_{9/2}$ to Er^{3+}:$^4I_{9/2}$ energy gap, making the Yb^{3+}:$^2F_{5/2}$ to Yb^{3+}:$^2F_{15/2}$ gap much harder to bridge with phonons. However, we also note that the change in lifetime of Yb^{3+}:$^2F_{5/2}$ cannot be simply explained by an increase in non-radiative rates. Rather the change in the lifetime of Yb^{3+}:$^2F_{5/2}$ is also associated with the

thermal equilibrium between the populations in Yb^{3+}:$^2F_{5/2}$ and the Nd^{3+}:^4F levels. As the equilibrium shifts toward a greater fraction of the excited-state population (at a given instant) occupying the Nd^{3+}:^4F levels, the rate of decay of this total population manifold will also increase (due to the increased amount of radiative emission from the Nd^{3+}:^4F levels). In this model, the lifetime of the Yb^{3+}:$^2F_{5/2}$, and the Nd^{3+}:$^4F_{5/2}$ level will be the same. Indeed, in Figure S5, Supporting Information, we confirm that the lifetimes of the Yb^{3+}:$^2F_{5/2}$, and the Nd^{3+}:$^4F_{5/2}$ states in our material remain identical to one another over the entire temperature range.

A simple model for the intensity of the Nd^{3+}:$^4F_{5/2}$ emission can be derived considering a two-level model wherein transfer from the lower to higher level is thermally-activated, but the rest of the rates are not. This leads to an expression that differs from the previous only in the sign of the exponential factor: $I(T) = \frac{A_1}{1 + A_2 \exp\left(\frac{\Delta_{E_2}}{k_B T}\right)}$ (for derivation see Figure S6, Supporting Information). The fit of the NIR data to such a highly simplified model is reasonable, and the Δ_{E_2} extracted is 1450 cm^{-1}. This is in reasonable agreement with the 1300 cm^{-1} gap between the Yb^{3+}:$^2F_{5/2}$ and the Nd^{3+}:$^4F_{3/2}$ levels; and the 1000 cm^{-1} gap between the Nd^{3+}:$^4F_{3/2}$ and Nd^{3+}:$^4F_{5/2}$ levels. This supports our hypothesis that the increase in the 825 nm emission is dominated by enhanced phonon-assisted transfer of the emitting levels from the lower-lying levels.

The model and data start to deviate from each other at high temperatures, as the increased non-radiative rates at high temperatures, which act to reduce the emission intensity, are not taken into account. These would counteract the increase in intensity due to better phonon-assistance of the transfer, and are likely to cause the decrease in the slope of the NIR intensity as a function of temperature starting around 750 K.

Although the extracted activation energy of this process is smaller, its slope at high temperatures is still greater than the 660 nm emission due to the opposite sign in the exponential term. Thus, the different natures of the processes leading to the two emission lines will lead to an enhanced variation of their ratio over an expanded temperature range.

The measured FIR at different temperatures, based on the averaged results of the mentioned heating-cooling cycles, are plotted as points in Figure 2c. The interpolated line is based on a polynomial fit. The opposing behavior of the UC emission intensities of Er^{3+} and Nd^{3+} leads to an impressive 600-fold variation of FIR of Nd^{3+} to Er^{3+}, I_{NIR}/I_{red}, as the temperature changes from 290 K up to 830 K. The observed variation of FIR is an order of magnitude higher than that of the reported values for rare-earth-based optical thermometers in the literature, such as Yb^{3+}/Er^{3+} (approximately sixfold),[23] Yb^{3+}/Nd^{3+} (approximately fivefold)[16] and Tb^{3+}/Pr^{3+} (approximately tenfold).[4a]

As an aside, we note that weak UC emission of Er^{3+} in green with maxima at 525 and 549 nm can be also observed in our material (see Figure S6, Supporting Information). These emissions stem from the transition of Er^{3+}:$^2H_{11/2} \rightarrow {}^4I_{15/2}$ (defined as "G1") and Er^{3+}:$^4S_{3/2} \rightarrow {}^4I_{15/2}$ (defined as "G2"), respectively. These two energy levels are also TCLs and frequently used for optical thermometry.[1a,c,24] The emission intensity of G2 gradually decreases with increasing temperatures, whereas G1 slightly increases with temperature up to ≈500 K and then decreases at higher temperatures (>500 K). As a result, the FIR of I_{G1}/I_{G2} gradually rises with temperature from 0.3 (298 K) to 2 (833 K). However, the degree of variation of I_{G1}/I_{G2} (approximately sixfold) is significantly lower than that of I_{NIR}/I_{red} (≈600-fold) in same temperature range of temperatures (298–833 K), and these emissions much weaker in our samples.

From the interpolation in Figure 2c, the S_a and S_r can be calculated. These are shown in Figure 2d. The S_a varies from 0.003 K^{-1} at 293 K to 0.62 K^{-1} at 753 K. To the best of our knowledge, this value is the highest reported value in literature and is for an order of magnitude higher than that of other lanthanide based optical thermometers. For example, it is ≈70 times higher than that of frequently reported Yb^{3+}/Er^{3+} UC pair, such as $La_2O_2S:Yb^{3+},Er^{3+}$ (0.008 K^{-1} 562 K),[1c] and at least several times greater than reported for optical thermometers based on other binary luminescent centers, such as $NaYF_4:Tb^{3+}/Eu^{3+}$ (0.012 K^{-1}),[25] $NaGd(MoO_4)_3:Pr^{3+}/Tb^{3+}$ (0.097 K^{-1} at 483 K)[4a] and $Sc_2O_3:Eu^{2+}/Eu^{3+}$ (0.08 K^{-1} at 267 K).[11] The S_r decreases only gradually with temperature from 1.8%·K^{-1} at 290 K down to 0.7%·K^{-1} at 800 K. The high S_r is maintained over an impressive range, staying above 1.0% K^{-1} until 700 K. This is shown in **Figure 3** and compared with other state-of-the-art luminescent thermometry materials. For systems based on single-ion TCLs, the S_r is calculated based on literature reports for Δ_E, whereas for dual emitter systems data for the relative sensitivity is directly taken from the literature. As observable in Figure 3, although other material systems can compete with (or exceed) the S_r of our system in temperature ranges on the order of 100 K, no other system can offer such a good S_r over such a wide temperature range. This maintenance of a high S_r over a wide temperature range makes the concept of using emissions with contrary dependence on temperature attractive, and should stimulate further research in this direction.

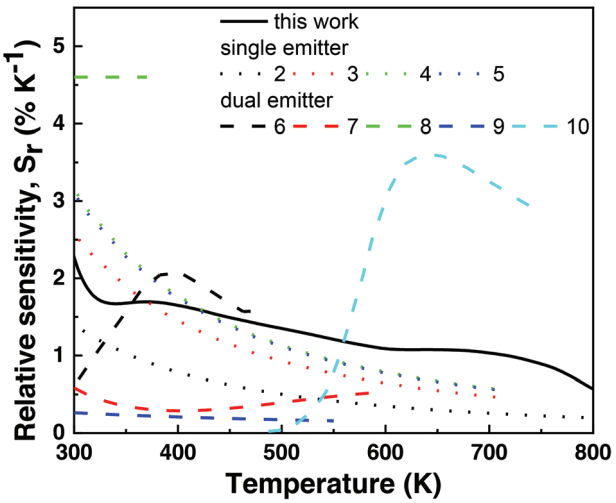

Figure 3. Comparison of the relative sensitivity, S_r, of state-the-art luminescent thermometers. Solid line: current work. Dotted lines (2–5) are previous work on TCLs from a single ion where relative sensitivity is calculated from reported Δ_E; 2,[26] 3,[6] 4,[8] and 5.[9] Dashed lines (6–10) are previous work using dual emission centers. S_r are directly extracted from literature reports; 6,[4a] 7,[12] 8,[13] 9,[10] 10.[15]

The uncertainty of the temperature estimation (δT) can be determined by Equation (5).[2a,13]

$$\delta T = \frac{1}{S_r} \times \frac{\delta \mathrm{FIR}}{\mathrm{FIR}} = \frac{\delta \mathrm{FIR}}{S_a} \tag{5}$$

where S is the relative or the absolute sensitivity and $\frac{\delta \mathrm{FIR}}{\mathrm{FIR}}$ is the relative error in the determination of FIR. For the temperature imaging demonstration below utilizing a scientific CMOS camera, we estimate $\frac{\delta \mathrm{FIR}}{\mathrm{FIR}} \approx 0.64\%\ \mathrm{Hz}^{-0.5}$ (see Note S8, Supporting Information). With $S_r \approx 1\%\ \mathrm{K}^{-1}$, $\delta T \approx 0.64\ \mathrm{K\ Hz}^{-0.5}$. This allows the temperature to be established within 2 K with a 100 ms exposure time. However, issues with image registration mean that the temperature uncertainty in our rough prototype is significantly poorer.

In order to illustrate the application of the LYEN material, the microcrystals were applied to the surface of a soldering iron tip. This was achieved in a simple fashion by pressing the tip into the phosphor powder. Images were then taken through a 600–700 nm band pass filter and a 750–850 nm band pass filter using a monochrome camera (Thorlabs, CS2100M-USB with MVL7000 lens). Unprocessed images showing the red and NIR images when the soldering iron heater is off are shown in **Figure 4**a,b respectively. These images reveal some of the practical challenges in thermal imaging with this micro powder phosphor. First, the intensity of the red and NIR emission differs significantly due to the non-uniformity of the coating. Bright spots are visible where larger clusters of the micro powder phosphor were deposited. However, once the FIR is taken, these features drop out and a smoothly varying FIR is obtained in Figure 4c. We note that the band pass filters in front of the camera were changed by hand, and slight differences in the angle-of-incidence due to the different seating positions of the filters in their holders lead to a slight change in the angle of the transmitted light which corresponds to a slight spatial offset in the red and NIR images. In order to compensate for this offset, image registration was performed using the "Registration Estimator" app in MATLAB (MATLAB R2019b, Mathworks). The complete processing script is provided in the supporting information, as is a schematic showing the experimental setup.

Nonetheless, the question arises why the FIR smoothly varies at a constant temperature? This is caused by the intensity variation across the excitation laser beam (approximately Gaussian), and the differing dependence of the 660 and 825 nm UC on the excitation power density. Whereas the 660 nm UC has an approximately quadratic dependence on the intensity at low excitation power densities (it is a two-photon process),[18] the thermally assisted 825 nm UC depends almost linearly on the excitation power density.[16] The results of this discrepancy are clearly visible in the images. The red emission in Figure 4a, is more tightly concentrated near the center-point of the excitation beam, the emission intensity drops more quickly toward the beam wings due to the nonlinear excitation power density dependence of the two-photon UC process. The NIR emission is more uniform, with the areas of the soldering iron head further from the beam center much more clearly visible. This causes variation in the FIR at a constant temperature as shown in Figure 4c. The NIR/red ratio increases symmetrically around the beam maximum (located ≈1/3 of the way from the tip).

This variation of the FIR at a single temperature needs to be accounted for, but does not negate the utility of our phosphor. As the tip is heated, the initial FIR at each location (determined at this constant temperature) will increase in the same fashion because the increase in NIR emission due to energy transfer, and the decrease in the red emission due to the increased non-radiative rates do not change with intensity. Therefore, it is sufficient to consider the relative increase in the FIR with temperature. To simply do this, we divide each pixel by a correction factor determined by the constant temperature FIR image, in order to bring each pixel to the FIR we expect at 293 K (again full details can be found in the MATLAB script in the Supporting Information).

The soldering iron heater can be roughly adjusted from a low to high setting. The raw images, in the red and NIR of the room temperature, low-heater setting, and high-heater setting are shown in Figure S9, Supporting Information. Here the images are all presented with the same grey scale map, so that the absolute intensity of the emissions can be compared. It is easy to see by eye that whereas the absolute intensity of the

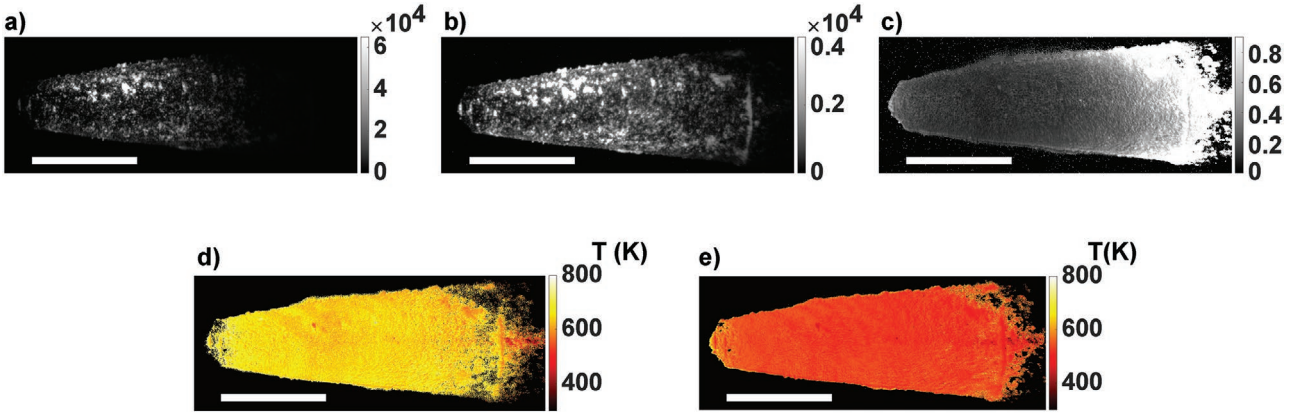

Figure 4. Images of the a) red and b) NIR emission at room temperature, c) calculated FIR for the soldering iron tip at room temperature. d) Soldering iron temperature based on analysis of FIR at a high heater setting, and e) at a low heater setting. White scale bars are 6 mm.

red decreases, that of the NIR increases. This is a compelling visual example of how the decrease versus increase of the absolute emission intensities makes this material a good temperature sensor, one does not have to strain to see a subtle change in ratio.

The temperature of the tip for the two heater settings is presented in Figure 4d,e. The data for the high setting is shown in Figure 4d where the average temperature for the tip taken from a ROI excluding the tip edges is 640 K and the standard deviation in the temperature determined over the same 50 000 pixel area is 20 K. Figure 4e shows the image for the lower heater setting, with an average temperature of 530 K and a standard deviation between the temperature measured for each pixel of 10 K. These initial demonstrations show the applicability of this phosphor for thermography. The considerable standard deviation of individual pixel values is still limited in this rough prototype by the strong spatial variation of intensity due to inhomogeneous coating of the marked object, and do not represent the fundamental limits for temperature resolution of the phosphor system. Fundamentally, it should be possible to determine temperature to within 0.6 K with a 1 s exposure time (see Note S8, Supporting Information). The object spatial resolution of the camera/sensor system is on the order of 10 µm, however, significant high frequency spatial inhomogeneity is present in the current simple implementation due to inaccuracies in image registration which would have to be overcome in order to push spatial and temperature resolution to their limits in a specific application scenario. Optimizing the phosphor deposition to achieve uniform brightness would also help in this respect, relaxing the requirement for such perfect registration.

4. Conclusions

We demonstrate that a ratiometric optical thermometer with good sensitivity over a very wide temperature range can be achieved by designing materials with well-separated emission lines that show opposite behaviors as a function of temperature. In the current case, triply-doped LYEN provides well-separated UC emission bands in 660 nm and NIR due to the Er^{3+} ($^4F_{9/2} \rightarrow {}^4I_{15/2}$) and Nd^{3+} (Nd^{3+}:$^4F_{7/2}/^4F_{5/2} \rightarrow {}^4I_{9/2}$) transitions respectively. The 660 nm UC of Er^{3+} decreases with increasing temperature (being dominated by thermal activation of non-radiative rates), whereas the NIR UC of Nd^{3+} shows the contrary behavior and increases with increasing temperature (dominated by phonon-assisted energy transfer). This leads to a ≈600-fold change in the FIR (I_{NIR}/I_{red}) from 290 to 800 K and a high S_r above 1% K^{-1} in the range 290–700 K. Specifically, the S_r is between 1.8–0.7% K^{-1} over the range 290–833 K. The combined features of excellent S_r across the broad temperature range, and the well-separated UC emission bands make the material attractive for general application in optical thermometry over a wide range of temperatures. For example, in determining the temperature of batch reaction vessels during the process cycle. More generally, this work demonstrates the power of the strategy of using an emission process that absolutely increased with temperature coupled to one that absolutely decreases with temperature to obtain high S_r over a wide temperature range. This concept could be extended to other temperature ranges and sensitivities utilizing emission from other phonon-assisted UC processes and thermally-quenched levels with different activation energies.

5. Experimental Section

The $Yb^3/Er^{3+}/Nd^{3+}$ triply-doped sample with a nominal composition of $La_{1.84}Yb_{0.12}Er_{0.02}Nd_{0.02}O_3$ (LYEN) was prepared by a high-temperature solid-state reaction at 1550 °C for 24 h in ambient conditions with two intermediate grinding steps. The synthesis route follows that described in detail in the previous publications.[16,18]The crystal structure of LYEN was studied by X-ray diffractometry (XRD, Bruker, D2 phase, Cu Kα radiation). The morphology and particle size of LYEN were investigated by scanning electron microscopy (SEM, Zeiss Supra 60 VP). The absorption properties of Yb^{3+}, Er^{3+}, and Nd^{3+} in LYEN were measured as the diffuse reflectance spectrum using a spectrophotometer (Perkin Elmer Lambda 950) equipped with an integrating sphere. The temperature dependent UC emission properties of LYEN in the temperature range of 293–833 K were measured in a custom-built optical system. UC emission spectra were detected by using a 980 nm continuous-wave (CW) laser diode (Thorlabs, L980P200 in a temperature stabilized mount TCLDM9) as an excitation source and an irradiance calibrated CCD spectrometer (Avantes, ULS2048) as a detector. Excitation power density on the investigated sample was set to be 1 W·cm^{-2}. LYEN powder was put into an alumina crucible with size of 6.5 mm outer diameter × 4.0 mm height, then the filled crucible was placed inside a thermal stage (Microptik BV MHS1200-V/G). The temperature of the thermal stage was controlled in the range of 293–833 K by a type S Pt-10% Rh/Pt thermocouple connected to a temperature controller (Microptik BV, MTDC600) having a temperature resolution of ±0.1 K. For a homogeneous distribution of the temperature among the whole sample, 5 min were timed after the temperature change on the thermal stage. Thermal emission of the sample, which starts to be remarkable at high temperatures, was measured with the blocked excitation and then correspondingly subtracted from the UC emission spectra.

Optical images were taken with a CMOS monochrome camera (Thorlabs, CS2100M-USB with MVL7000 lens) with 16 bit depth. Calculations of the FIR were done also in 16 bit resolution. Excitation power density was same as that used for UC spectra detection (1 W·cm^{-2}). This was achieved by expanding a 1 W 980 nm beam from a CW titanium sapphire laser (SolsTiS, M2). The red emission of the Er^{3+} was detected using a combination of 600 nm long pass (Thorlabs, FEL0600) and 700 nm short pass filters (Thorlabs, FES0700), placed in front of the camera objective. The NIR emission of the Nd^{3+} was detected with a 750 nm long pass filter and short pass 850 nm (Thorlabs, FEL0750, and FES0850). A 950 nm short pass filter (Semrock, SEM-FF01-950/SP-25) was used for all measurements to additionally suppress scattered excitation light. The camera was placed at a distance of 20 cm from the soldering iron tip, and arranged to minimize the angle between the pointing of the camera lens and the excitation laser beam. This allowed the soldering tip surface on which the excitation laser impinged to be imaged. A schematic of the experimental setup is shown in Figure S10, Supporting Information. Exposure times of 100 ms were used to take the images.

Supporting Information

Supporting Information is available from the Wiley Online Library or from the author.

Acknowledgements

The authors gratefully acknowledge financial support by Technology Transfer Project N038 between KIT and Polysecure GmbH (Freiburg, Germany). Further financial support was provided by the Helmholtz Association: i) the Recruitment Initiative Fellowship for BSR; ii) the Science and Technology of Nanosystems (STN) program, and iii)

the Helmholtz Energy Materials Foundry (HEMF) project. Ngei Katumo and Reetu Elza Joseph acknowledge the Deutscher Akademischer Austausch Dienst (DAAD) for their Ph.D. scholarship. Eduard Madirov acknowledges the scholarship of the President of the Russian Federation for financial support.

Open access funding enabled and organized by Projekt DEAL.

Conflict of Interest

The authors declare no conflict of interest.

Keywords

lanthanide ions, luminescent thermometry, thermography, up-conversion emission

Received: November 3, 2020
Revised: November 27, 2020
Published online:

[1] a) J. Cao, F. Hu, L. Chen, H. Guo, C. Duan, M. Yin, *J. Am. Ceram. Soc.* **2017**, *100*, 2108; b) W. Xu, H. Qi, L. Zheng, Z. Zhang, W. Cao, *Opt. Lett.* **2015**, *40*, 5678; c) Y. Yang, C. Mi, F. Yu, X. Su, C. Guo, G. Li, J. Zhang, L. Liu, Y. Liu, X. Li, *Ceram. Int.* **2014**, *40*, 9875; d) W. Xu, Q. Song, L. Zheng, Z. Zhang, W. Cao, *Opt. Lett.* **2014**, *39*, 4635; e) X.-d. Wang, O. S. Wolfbeis, R. J. Meier, *Chem. Soc. Rev.* **2013**, *42*, 7834.

[2] a) C. D. S. Brites, A. Millán, L. D. Carlos, in *Handbook on the Physics and Chemistry of Rare Earths*, Vol. *49* (Eds: J.-C. G. Bünzli, V. K. Pecharsky), Elsevier, New York **2016**, p. 339; b) X. Wang, Q. Liu, Y. Bu, C.-S. Liu, T. Liu, X. Yan, *RSC Adv.* **2015**, *5*, 86219; c) M. Quintanilla, L. M. Liz-Marzán, *Nano Today* **2018**, *19*, 126.

[3] S. F. Collins, G. W. Baxter, S. A. Wade, T. Sun, K. T. V. Grattan, Z. Y. Zhang, A. W. Palmer, *J. Appl. Phys.* **1998**, *84*, 4649.

[4] a) Y. Gao, F. Huang, H. Lin, J. Zhou, J. Xu, Y. Wang, *Adv. Funct. Mater.* **2016**, *26*, 3139; b) O. A. Savchuk, J. J. Carvajal, C. D. S. Brites, L. D. Carlos, M. Aguilo, F. Diaz, *Nanoscale* **2018**, *10*, 6602; c) B. Dong, B. Cao, Y. He, Z. Liu, Z. Li, Z. Feng, *Adv. Mater.* **2012**, *24*, 1987.

[5] M. D. Dramićanin, *Methods Appl. Fluoresc.* **2016**, *4*, 042001.

[6] L. R. Đačanin, M. D. Dramićanin, S. R. Lukić-Petrović, D. M. Petrović, M. G. Nikolić, *Radiat. Meas.* **2013**, *56*, 143.

[7] H. Suo, F. Hu, X. Zhao, Z. Zhang, T. Li, C. Duan, M. Yin, C. Guo, *J. Mater. Chem. C* **2017**, *5*, 1501.

[8] W. Xu, X. Gao, L. Zheng, Z. Zhang, W. Cao, *Sens. Actuators, B* **2012**, *173*, 250.

[9] X. Tian, X. Wei, Y. Chen, C. Duan, M. Yin, *Opt. Express* **2014**, *22*, 30333.

[10] D. Chen, S. Liu, Z. Wan, Z. Ji, *J. Phys. Chem. C* **2016**, *120*, 21858.

[11] Y. Pan, X. Xie, Q. Huang, C. Gao, Y. Wang, L. Wang, B. Yang, H. Su, L. Huang, W. Huang, *Adv. Mater.* **2018**, *30*, 1705256.

[12] C. D. S. Brites, K. Fiaczyk, J. F. C. B. Ramalho, M. Sójka, L. D. Carlos, E. Zych, *Adv. Opt. Mater.* **2018**, *6*, 1701318.

[13] M. Sekulić, V. Đorđević, Z. Ristić, M. Medić, M. D. Dramićanin, *Adv. Opt. Mater.* **2018**, *6*, 1800552.

[14] I. E. Kolesnikov, D. V. Mamonova, A. A. Kalinichev, M. A. Kurochkin, V. A. Medvedev, E. Y. Kolesnikov, E. Lähderanta, A. A. Manshina, *Nanoscale* **2020**, *12*, 5953.

[15] M. N. Getz, O. Nilsen, P.-A. Hansen, *Sci. Rep.* **2019**, *9*, 10247.

[16] R. E. Joseph, D. Busko, D. Hudry, G. Gao, D. Biner, K. Krämer, A. Turshatov, B. S. Richards, I. A. Howard, *Opt. Mater.* **2018**, *82*, 65.

[17] C. Mi, J. Zhou, F. Wang, D. Jin, *Nanoscale* **2019**, *11*, 12547.

[18] G. Gao, D. Busko, S. Kauffmann-Weiss, A. Turshatov, I. A. Howard, B. S. Richards, *J. Mater. Chem. C* **2017**, *5*, 11010.

[19] A. Sedlmeier, D. E. Achatz, L. H. Fischer, H. H. Gorris, O. S. Wolfbeis, *Nanoscale* **2012**, *4*, 7090.

[20] B. Wu, M. Zinkevich, F. Aldinger, D. Wen, L. Chen, *J. Solid State Chem.* **2007**, *180*, 3280.

[21] R. E. Joseph, C. Jiménez, D. Hudry, G. Gao, D. Busko, D. Biner, A. Turshatov, K. Krämer, B. S. Richards, I. A. Howard, *J. Phys. Chem. A* **2019**, *123*, 6799.

[22] a) Y. Shen, J. Lifante, N. Fernández, D. Jaque, E. Ximendes, *ACS Nano* **2020**, *14*, 4122; b) X. Qiu, Q. Zhou, X. Zhu, Z. Wu, W. Feng, F. Li, *Nat. Commun.* **2020**, *11*, 4; c) A. Bednarkiewicz, L. Marciniak, L. D. Carlos, D. Jaque, *Nanoscale* **2020**, *12*, 14405.

[23] a) S. Liu, H. Ming, J. Cui, S. Liu, W. You, X. Ye, Y. Yang, H. Nie, R. Wang, *J. Phys. Chem. C* **2018**, *122*, 16289; b) S. Fan, G. Gao, S. Sun, S. Fan, H. Sun, L. Hu, *J. Mater. Chem. C* **2018**, *6*, 5453.

[24] R. G. Geitenbeek, P. T. Prins, W. Albrecht, A. van Blaaderen, B. M. Weckhuysen, A. Meijerink, *J. Phys. Chem. C* **2017**, *121*, 3503.

[25] M. Ding, M. Xu, D. Chen, *J. Alloys Compd.* **2017**, *713*, 236.

[26] G. Gao, D. Busko, S. Kauffmann-Weiss, A. Turshatov, I. A. Howard, B. S. Richards, *J. Mater. Chem. C* **2018**, *6*, 4163.